A novel tactile sensing skin for surface perception

Subham Das[1], Mitradip Bhattacharjee[1,*], Karthick Thiyagarajan[2], and Sarath Kodagoda[3]

[1]i-Labs, Electrical Engineering and Computer Science, Indian Institute of Science Education and Research Bhopal, Madhya Pradesh, 462066, India.
[2]School of Engineering, Design and Built Environment, Western Sydney University, Kingswood, Western Sydney, New South Wales, 2747, Australia.
[3]UTS Robotics Institute, University of Technology Sydney, Ultimo, Sydney, New South Wales, 2007, Australia
[*]Corresponding author: mitradip@iiserb.ac.in

ABSTRACT

Humans employ a fusion of pressure and temperature signals to perceive tactile stimuli. While replicating the complexity of human tactile sensing poses challenges, advancements in artificial tactile sensing skins play a crucial role in the progress of robotics and prosthetics. Here, we present a novel tactile sensing skin designed for the perception of diverse surfaces. It utilizes a microstructured porous tactile sensor, exhibiting notable sensitivity at 21.5 kPa^{-1} under low-pressure conditions and 2.5 kPa^{-1} in high-pressure scenarios. The sensor also boasts an impressively low detection limit of 50 kPa, allowing for discernment of subtle pressure variations. Simultaneously, we utilize a flexible temperature sensor exhibiting a sensitivity of 0.58 $\% \ C^{-1}$ and swift response attributes to facilitate the detection of radiated heat from diverse surfaces. The incorporation of a multilayer perceptron algorithm into the developed glove-like system, equipped with tactile and temperature sensors, achieves 87% accuracy in classifying eleven distinct surfaces.

Introduction

In the rapidly advancing field of robotic science and technology, a growing number of intelligent systems are being employed to substitute for humans in tasks conducted in intricate environments or to aid human activities through prosthetics. Attaining a thorough comprehension of the surroundings, recognizing potential threats, and executing complex motor tasks may all require the incorporation of multimodal tactile perception. The replication of sophisticated, skin-like tactile capabilities holds significant importance in enabling advanced robotic systems[1] and prosthetic devices[2] to function with precision and adaptability. Identification of surfaces plays a crucial role in empowering autonomous mobile robots to navigate challenging and unstructured environments[3]. The real-time recognition of diverse terrain surfaces and the capability to perceive ground texture enable robots to dynamically adjust their trajectories, ensuring safer and more efficient movement[4]. Artificial neural network-based methods have been extensively explored for precise surface recognition, showing potential applications in prosthetic devices and the medical field[5,6]. Existing techniques, such as stereo cameras[7], infrared rangefinders[8], and 3D laser scanners[9], face limitations in terms of weight, real-time processing, and suitability for prosthetics. Technological advancements in virtual reality present opportunities for wearable devices that offer somatosensory feedback, enhancing perception in virtual environments[10]. For finger motion tracking, various solutions are currently employed, including rigid systems with cameras[11] and inertial measuring units[12], as well as flexible approaches utilizing resistivity, capacitance, and optics[13,14]. Sensing mechanisms like piezoresistance, piezocapacitance, triboelectricity, piezoelectricity, thermoelectricity, and pyroelectricity are widely adopted, providing advantages in developing portable and sustainable systems with reduced power consumption[15].

Considerable focus has been dedicated to extensively exploring the tensile strength and physical characteristics of polymers, which have widespread applications and serve diverse purposes[16,17]. One specific subset within the extensive realm of polymers that has attracted significant attention is conductive polymers, owing to their remarkable potential for sensor-based applications. These polymers demonstrate intriguing properties similar to semiconductive materials, making them particularly suitable for sensing mechanisms[18]. Among the various conductive polymers, prominent choices for healthcare technologoes or robotic applications include polyimide (PI), polyaniline (PANI), polydimethylsiloxane (PDMS), polyethylene terephthalate (PET), and poly(3,4-ethylenedioxythiophene) (PEDOT:PSS)[19,20]. These polymers have gained prominence due to their exceptional features such as remarkable biocompatibility, inherent biodegradability, impressive optical transparency, and electrical behavior[21]. These distinctive attributes position these materials at the forefront of biomedical research, leading to their integration into a wide range of cutting-edge applications.

This study centers on the potential of soft polymer-based tactile sensors to enhance perception and transform surface identification. Leveraging the innate sensitivity of our proposed tactile sensing skin to contact pressure enables the discernment of crucial surface attributes such as material hardness and roughness. Additionally, the integration of temperature sensors empowers the capture of radiant heat signatures emitted by distinct surface types, thereby improving the reliability of surface detection. Our sensing system design features a seamless integration of multiple sensors, effectively avoiding any detrimental cross-coupling artifacts that might compromise performance. To demonstrate the sensing capability, we devised a glove arrangement with an array of sensors, skillfully imparting a lifelike semblance of tactile abilities. A key element in achieving accurate surface classification involves synergistically amalgamating the tactile sensing data with a machine learning algorithm.

In this study, we demonstrate a novel tactile sensing skin designed for surface perception. The sensing skin incorporates a porous piezocapacitive tactile sensor that was fabricated using a zinc oxide-polydimethylsiloxane (ZnO-PDMS) composite, showcasing an exceptional sensitivity of 21.5 kPa^{-1} under low-pressure conditions and 2.5 kPa^{-1} under high pressure conditions. Additionally, a resistive temperature sensor based on graphene oxide and PEDOT:PSS (GO+PEDOT:PSS) formulation was developed, demonstrating a sensitivity of 0.58 $\%C^{-1}$. The acquired sensor data were processed and input into an artificial neural network algorithm, specifically a multilayer perceptron (MLP), to enable accurate classification of various surface types. The MLP algorithm exhibited remarkable efficacy, achieving a high accuracy of approximately 87% in surface classification. The proposed tactile sensing skin holds potential applications in areas such as smart prosthetics and robotics. Figure 1 presents a visual representation of the proposed methodology, illustrating the integration of fabricated sensors and the surface classification framework.

Results

The evaluation of the tactile sensing skin's ability to accurately capture signals related to pressure, temperature, and time is crucial in comprehensive analyses. Parameters such as sensitivity, detection limit, dynamic range, response time, and relaxation time are pivotal in assessing the sensing skin's effectiveness in pressure and temporal resolution. Sensitivity, in particular, is significant, representing the ratio of the change in the measured quantity (Q) to the corresponding change in the output signal (S) relative to the initial signal (S_0). The equations for calculating these parameters are concisely presented and explained in section I-S2 of the electronic supporting material (ESI).

Tactile sensor response and performance on varied surfaces. The developed tactile sensor was carefully positioned on diverse surfaces, and controlled pressure was applied to capture the corresponding capacitance readings using an LCR meter (Hioki IM3536); these readings were subsequently normalized (C/C_0). To establish low-pressure conditions, we utilized precisely calibrated weights ranging from 0.1 to 2 kPa. Simultaneously, a specially designed pressure application apparatus, boasting a resolution of 0.2 kPa and a maximum pressure capacity of 300 kPa, was employed for scenarios involving higher pressures. In the initial experimental phase, a constant pressure of 5 kPa was applied to the sensor across ten distinct surface types. Following this, a frequency sweep spanning from 1 kHz to 8 MHz was conducted to investigate any potential frequency-related influence on the measured capacitance. A comprehensive analysis of the plots obtained in Figures 2A and 2B revealed negligible frequency-dependent effects on capacitance. These results validate the assertion outlined in Equation (4) (section I-S3 of ESI), which suggests the absence of frequency dependence in capacitance.

The data collection process comprises two distinct phases to enable comprehensive analysis. The first phase investigates the sensor's capacitance behavior under different surfaces and loading conditions. In the absence of pressure, capacitance values exhibit stochastic fluctuations within a modest range of approximately 0.5 pF. However, as applied pressure increases, noticeable variations in capacitance become apparent. A deeper analysis, capturing mean values and coefficient of variation (CoV) (Figure 2A(iii) and 2A(iv)), illuminates underlying trends. Surfaces with higher hardness demonstrate higher mean responses, exemplified by rocks and pebbles, exhibiting a capacitance value of approximately 6 pF. Conversely, softer surfaces, such as mud and grass, show relatively lower response levels, with a capacitance value of around 3.25 pF. Rougher surfaces manifest greater deviation from the mean, indicated by larger error bars associated with surfaces like sponges and pebbles, demonstrating a deviation of around 14%. In contrast, smoother surfaces, like sand and tile, exhibit minimal variation of approximately 2%. These observations facilitate effective discrimination of diverse surfaces and provide a foundation for machine learning algorithms to utilize these discernible patterns for accurate predictions.

In the subsequent phase, a subset of three distinct materials—tile, sponge, and sand—was chosen, each characterized by unique surface attributes. Tile features a smooth and rigid surface, sponge presents a rough and pliable texture, and sand is known for its smooth and yielding composition. These materials were employed in a series of experiments, where incremental pressures ranging from 1 kPa to 100 kPa were applied to the sensor surface at three discrete frequencies (8 MHz, 1 MHz, and 500 kHz).

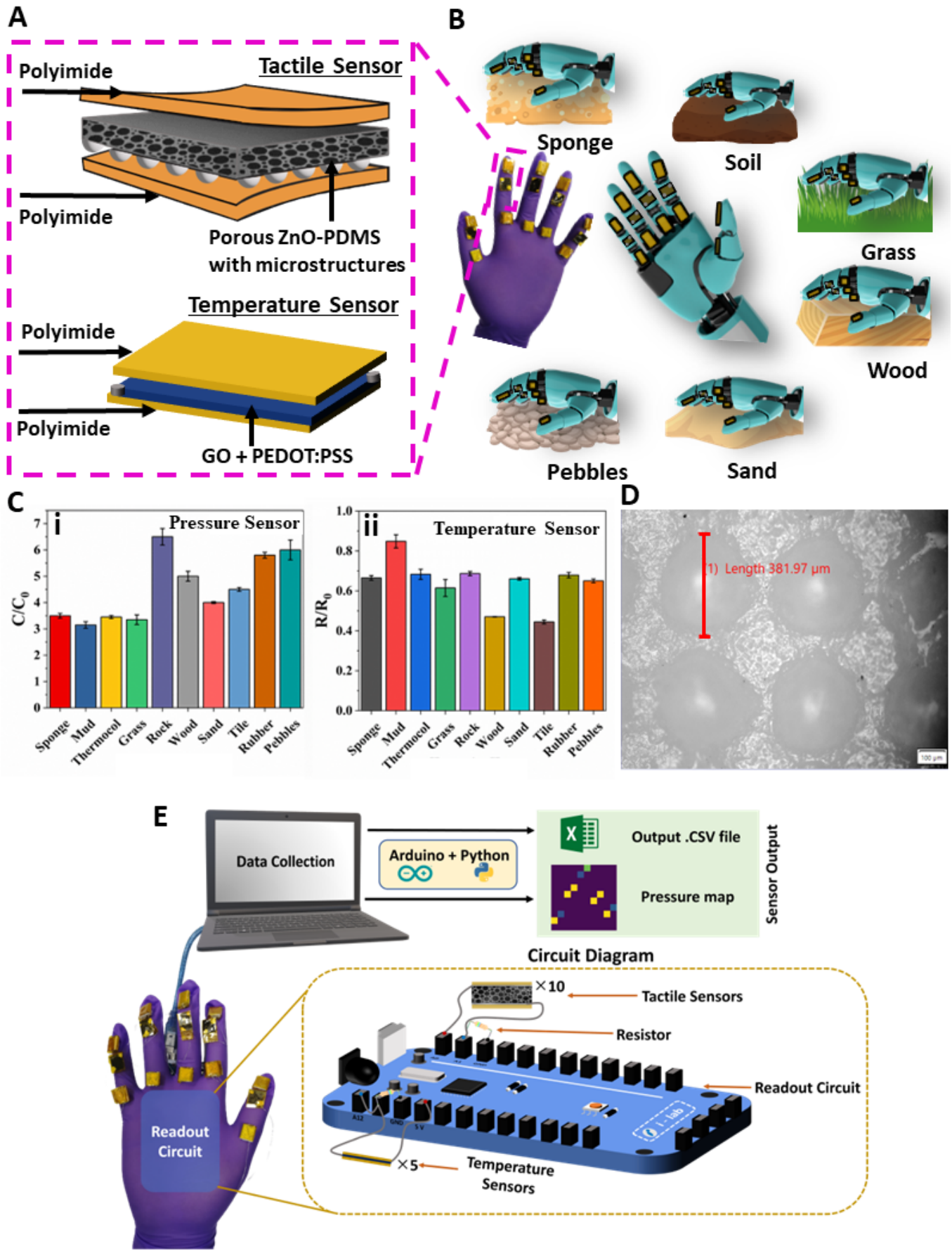
A
Polyimide
Tactile Sensor
Polyimide
Porous ZnO-PDMS
with microstructures
Temperature Sensor
Polyimide
Polyimide
GO + PEDOT:PSS
B
Sponge
Soil
Grass
Wood
Pebbles
Sand
C
i
Pressure Sensor
C/C0
Sponge
Mud
Thermocol
Grass
Rock
Wood
Sand
Tile
Rubber
Pebbles
ii
Temperature Sensor
R/R0
D
1) Length 381.97 µm
E
Data Collection
Arduino + Python
Output .CSV file
Pressure map
Sensor Output
Circuit Diagram
×10
Tactile Sensors
Resistor
Readout Circuit
×5
Temperature
Sensors
Readout
Circuit

Figure 1. Schematic representation summarizing the work conducted: (A) Depiction of the fabricated tactile and temperature sensors. (B) Future potential for integrating the fabricated sensors with robotic systems or smart prosthetic for surface type identification. (C) Plotting the response of the two sensors on different surfaces. (D) Optical microscope image (10X zoom) showcasing the microstructures in the ZnO-PDMS tactile sensor, and (E) Utilization of an integrated sensor-glove setup for surface recognition. The setup includes ten piezocapacitive tactile and five piezoresistive temperature sensors connected to a readout circuit, enabling data collection, storage in a .csv file, and visual display of the output as a pressure map.

The sensor's response to the applied pressure on the mentioned surfaces is illustrated in Figure 2B(i) and 2B(ii). Each material demonstrates a discernible response pattern that remains distinct and non-overlapping. Moreover, the influence of frequency on the sensor's response is determined to be negligible, as the plots display significant overlap, indicating the absence of frequency-dependent effects. Figure 2B(iii) and 2B(iv) provide comprehensive details regarding the CoV and mean values as a function of increasing pressure, respectively. The sensor exhibits a higher response with higher pressure levels, accompanied by reduced deviation from the mean. This behavior arises because the sensing layer approaches its compressional limit, limiting the available thickness for compression. Conversely, under low-pressure conditions, a greater extent of thickness is available for compression, resulting in a comparatively higher degree of deviation from the mean response.

The response behavior of microstructured PDMS utilized in tactile sensing applications displays nonlinearity attributed to the compressive strain relationship. This nonlinear characteristic arises from the rapid deformation of PDMS, resulting in an initial high sensitivity that gradually decreases over time due to mechanical saturation. The response curve and sensitivity plot are depicted in Figure 2B(iv). In the low-pressure range (1 - 5 kPa), a notable sensitivity of 21.5 kPa^{-1} is observed, while the moderate-pressure range (25 - 100 kPa) exhibits a sensitivity of 8.6 kPa^{-1}. The high-pressure range (150 - 300 kPa) displays a sensitivity of 2.5 kPa^{-1}. These remarkable sensitivities are primarily attributed to key enhancing factors, including the creation of porosity through CAM, the utilization of hemispherical microstructures, and the incorporation of ZnO into the PDMS matrix. The incorporation of ZnO into the PDMS matrix is particularly significant, imparting the sensor with a linear and heightened sensitivity across a broader pressure range. The response curve of the sensor necessitates fitting multiple linear segments to delineate distinct sensitivity ranges or dynamic regimes. In Figure 2B(iv), three discernible sensitivity ranges are observed along with their respective sensitivities, and the values are summarized in Table 1A.

The second phase of our investigation involves a comprehensive temporal analysis of the developed tactile sensors. To examine the sensor's dynamic response under increasing pressure, we utilized an Arduino Mega microcontroller to meticulously record capacitance readings. A detailed description of sensor-circuit integration is provided in section II-S4 of ESI. For this analysis, a carefully curated selection of four distinct surfaces was chosen. The findings presented in Figure 2C reveal striking dissimilarities in the sensor's response patterns across the diverse pressure regimes and surface types examined. Surfaces characterized by higher hardness, namely plastic, and tile, elicit a pronounced response from the sensor, with capacitance values reaching approximately 12 pF. These surfaces exhibit remarkable consistency in their response profiles, attributed to their inherently smooth texture. In stark contrast, the sensor's response to the same applied pressure on sponge and sand surfaces is comparatively diminished, yielding capacitance values of around 9 pF. The rough and irregular surface of the sponge introduces a heightened degree of variability in the sensor's output. Conversely, the more uniform and smoother surface of sand engenders a relatively stable response. The results of the temporal analysis closely align with the outcomes derived from the static experiments. This convergence of findings strengthens our confidence in the consistency and reliability of the sensor's behavior across various experimental conditions, attesting to the robustness and validity of our research outcomes.

Temperature sensor response and performance evaluation. Since GO+PEDOT:PSS is sensitive to both pressure and temperature[27,28], relying on resistance readings due to surface temperature alone would be inaccurate, given the influence of applied pressure. To address this, the temperature sensor was positioned separately next to the tactile sensor at a depth of 2 mm (the thickness of the tactile sensor) to ensure no contact with the surface. Resistance readings from radiative heat were normalized and plotted (Figure 3A) for analysis. The sensor's sensitivity was calculated to be 0.58 $\%C^{-1}$, demonstrating linear characteristics ($R^2 \sim 0.98$), consistent with literature[28], as depicted in Figure 3B. Finally, the sensor's performance was evaluated in terms of response and recovery time (Figure 3C). With a response time of approximately 40 seconds, the flexible temperature sensor exhibits remarkable sensitivity to temperature fluctuations. After being withdrawn from the hotplate (at 80°C) and left at room temperature to cool down, the sensor demonstrated a recovery time of around 60 seconds. In comparison, a commercial sensor took approximately 62 seconds to respond and about 120 seconds to fully recover, while the GO+PEDOT:PSS sensor fully recovered within 60 seconds. Consequently, when compared to a conventional thermistor, the printed GO+PEDOT:PSS-based temperature sensor demonstrated faster response times.

Table A. Sensitivity of tactile sensor across various ranges.

Substrate	**Active Sensing Material**	**Modification**	**Sensitivity** (kPa^{-1})	**Range** (kPa)
PI	PDMS + ZnO	Porous + Hemispherical microstructures	21.531	1 - 5
			8.612	25 - 100
			2.512	150 - 300

Table B. Performance of various classification algorithms on the obtained dataset.

Sno.	**Classification Algorithm for Surface Perception**	**Accuracy (%)**
1.	Random Forest	56.04
2.	Decision Tree	42.00
3.	Logisitc Regression	42.83
4.	K-means clustering	30.67
5.	Support Vector Machines (SVM)	55.64
6.	1D Convolutional Neural Network	82.48
7(a).	MLP - All Data	87.00
7(b).	MLP - without capacitance data	52.86
7(c).	MLP - without resistance data	58.26
7(d).	MLP - without applied pressure data	81.79

Table C. Classification analysis and F_1 score

Surface Type	**Precision**	**Recall**	**F_1 score**	**Support**
Tile	0.99	1.00	1.00	213
Sponge	0.83	0.90	0.86	200
Balloon	1.00	1.00	1.00	22
Thermocol	0.93	0.75	0.83	207
Rock	0.81	0.87	0.84	192
Sand	0.81	0.86	0.83	211
Wood	1.00	0.99	1.00	210
Grass	0.77	0.74	0.75	198
Mud	0.77	0.83	0.80	199
Pebbles	0.80	0.79	0.79	202
Rubber	0.93	0.88	0.90	201

Table D. Comparison with flexible piezocapacitive sensors reported in previous literature.

Sno.	**Material of the Dielectric Layer**	**Average Sensitivity** (kPa^{-1})	**Limit of Detection** (kPa)	**References**
1.	Melamine Sponge	0.477	0.5	[22]
2.	PDMS	0.0635	2	[23]
3.	AgNP microstructured PDMS	0.48	1	[24]
4.	Ecoflex	0.032	1.5	[25]
5.	ZnO-PDMS	0.22	150	[26]
6.	Porous microstructured ZnO-PDMS	10.885	50	**Our work**

Table 1. Tabular summary of obtained data and comparisons with previous works.

Multilayer perceptron classifier for surface perception. The data acquisition process involved capturing information from the tactile and temperature sensors, leading to the creation of an extensive dataset encompassing 11 distinct surface types. This dataset includes crucial parameters such as capacitance, resistance, and applied pressure, totaling 10,168 recorded data points. Each surface type was represented by a set of approximately 1000 data entries, ensuring robust statistical representation. To ensure an unbiased assessment, a random 80% of the dataset was used for testing, while the remaining 20% served as the training set. Through the utilization of various classification-based machine learning algorithms, significant optimization efforts were undertaken to maximize their performance. The resulting accuracies achieved by these algorithms are detailed in Table 1B. Remarkably, the Multilayer Perceptron (MLP) algorithm emerged as the most adept, demonstrating a high accuracy of 87%.

The data collection process from the setup (Figure 4A) is succeeded by analysis and classification using the obtained data. The performance evaluation of the evaluated models involved constructing a confusion matrix to comprehensively assess the accuracy of surface classification. This matrix visually depicts the correct and incorrect classifications of identified surfaces based on values of TP (true positive), TN (true negative), FP (false positive), and FN (false negative). Figure 4B presents the generated confusion matrix, providing insights into distinct scenarios for analysis. In the base case scenario, as depicted in Figure 4B(i), where all sensor parameters were considered, a high accuracy of 87% was achieved. Interestingly, when omitting the capacitance values obtained from the tactile sensor (Figure 4B(iii)), the accuracy witnessed a substantial reduction to 52.86%. Similarly, the exclusion of the resistance data captured by the temperature sensor (Figure 4B(iv)) resulted in a diminished accuracy of 58.26%. These observations underscore the pivotal role played by the capacitance data derived from pressure changes, as it emerges as a critical factor in accurately identifying various surfaces. Meanwhile, the resistive data derived from temperature changes provides supplementary information that augments classification accuracy. Furthermore, it is noted that even in the absence of knowledge regarding the applied pressure, the surface detection accuracy remained high, reaching 82% (Figure 4B(ii)). These findings emphasize that knowledge of applied pressure alone is inadequate to discern the nature of the surface, and the collective contributions of all three sensors are essential for achieving the best prediction accuracy.

The loss curve (Figure 3C), a crucial diagnostic tool extensively utilized in neural network analysis, holds significance in understanding the intricate dynamics of the training process and the network's learning behavior. The steepness of the curve serves as a measure of learning efficacy, with a steeper curve corresponding to minimized information loss. In Figure 3C, we observe a gradual reduction in curve steepness, indicating an escalating impact of removed information on the algorithm's classification capacity. This phenomenon hampers the algorithm's ability to effectively train itself and acquire essential knowledge. During model evaluation, individual data instances, comprising input features and their corresponding labels denoted as "actual output" or "expected output," are fed into the model. The model generates predicted outputs based on these inputs, facilitating the computation of the loss function.

The computation of F_1 scores for each surface category was undertaken, recognizing that relying solely on the accuracy metric can be misleading. Accuracy merely reflects the percentage of correctly classified data points, overlooking misclassified instances in datasets and those affected by class imbalance. The F_1 score provides valuable insight and reliable metrics into the accuracy of classifications. The results (Table 1C) revealed a reasonably high level of precision across most surfaces, with the vast majority surpassing 80% accuracy. Even in the case of grass, which exhibited the lowest F_1 score, the classified performance remained commendable, with an accuracy rate of 75%. To explore the algorithm's resilience and adaptability, the dataset deliberately incorporated "balloon" as a class, characterized by its inherent data imbalance. Despite comprising a mere 22 data points, this limited representation proved sufficiently robust, enabling the algorithm to achieve a flawless classification accuracy of 100% midst the expansive array of 10,000 data points. This outcome demonstrates the algorithm's capability in accommodating diverse data distributions and its potential to excel in real-world applications.

Discussion

Sensor technologies have extensively utilized materials such as lead zirconate titanate (PZT), barium titanate ($BaTiO_3$), aluminum nitride (AlN), and gallium nitride (GaN)[29,30]. However, their fabrication involves significant costs and time investment, and many of these materials lack eco-friendly or biocompatible attributes. In contrast, ZnO has emerged as a promising alternative due to its easy production and non-toxic characteristics. The incorporation of ZnO nanoparticles into polymers has been demonstrated to greatly enhance toughness, scratch resistance, fatigue resistance, thermal stability, weatherability, as well as optical and barrier properties, expanding the range of potential applications[31,32]. Furthermore, combining ZnO with PDMS imparts biocompatibility and environmental friendliness, ensuring safe disposal in landfills[33,34]. While silver nanoparticles (AgNP) have been considered as an alternative to ZnO[35], their high cost, complex synthesis procedures, and comparable or inferior sensitivity improvements compared to ZnO-PDMS tactile sensors make them less desirable. Ex-

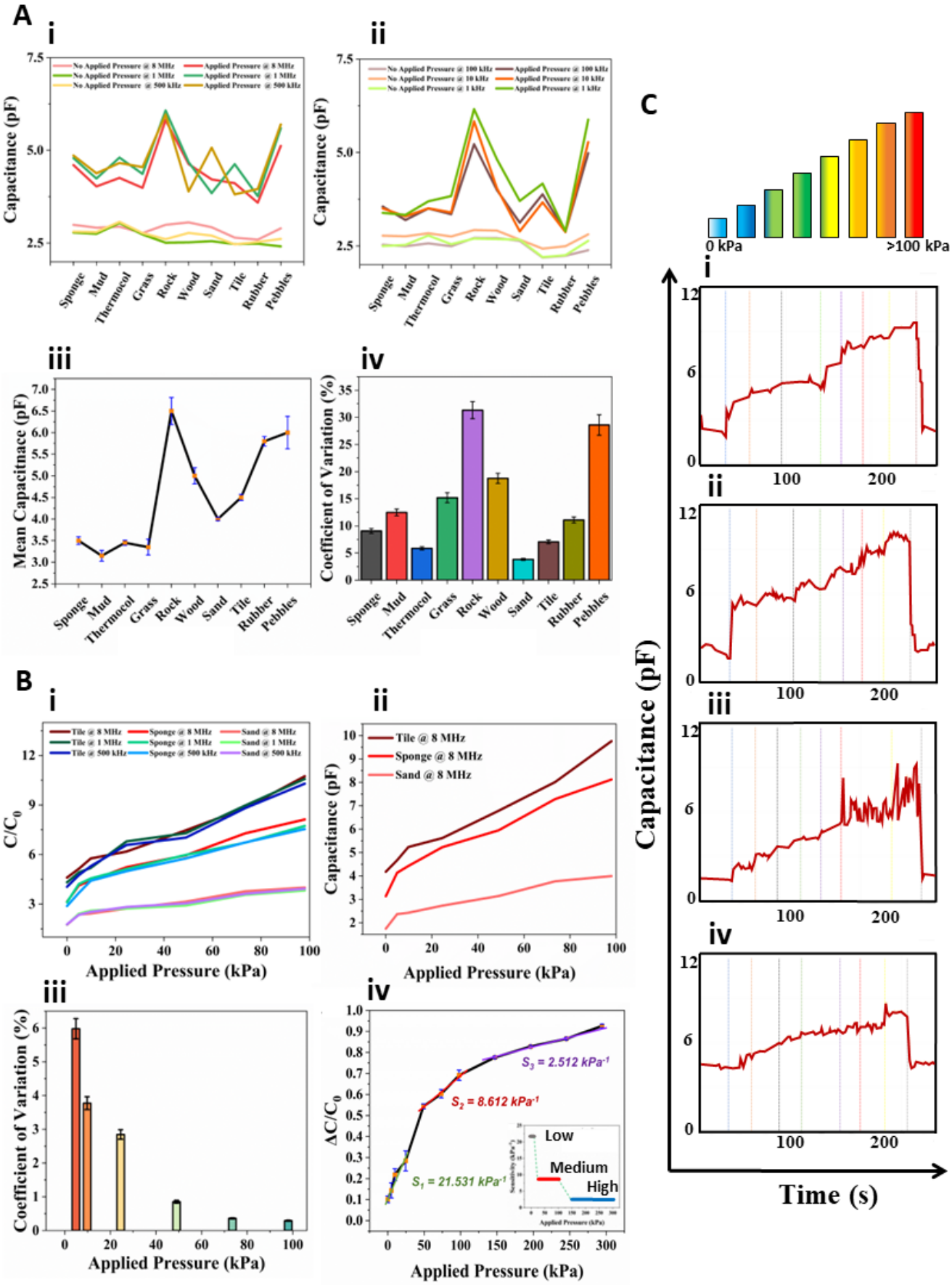
A
i
ii
iii
iv
Capacitance (pF)
Mean Capacitnace (pF)
Coefficient of Variation (%)
Sponge
Mud
Thermocol
Grass
Rock
Wood
Sand
Tile
Rubber
Pebbles
B
i
ii
iii
iv
C/C0
Capacitance (pF)
Applied Pressure (kPa)
Tile @ 8 MHz
Sponge @ 8 MHz
Sand @ 8 MHz
ΔC/C0
S1 = 21.531 kPa-1
S2 = 8.612 kPa-1
S3 = 2.512 kPa-1
Low
Medium
High
C
0 kPa
>100 kPa
Capacitance (pF)
Time (s)

Figure 2. (A) The response of the piezocapacitive tactile sensor on different surfaces is depicted as follows: (i) and (ii) Illustrates the sensor's response for a fixed pressure of 5 *kPa* and decreasing frequency from 8 *MHz* to 1 *kHz*, along with the corresponding response with no applied pressure. (iii) Presents the mean and standard deviation (error) of normalized capacitance on different surfaces. (iv) Provides information on the coefficient of variation (CoV) of capacitance readings for different surfaces. (B) The response of the piezocapacitive tactile sensor with increasing pressure for three distinct surfaces is presented: (i) and (iii) Depicts the sensor's response for a smooth hard surface (tile), a soft rough surface (sponge), and a smooth soft surface (sand) for three different frequencies. (iii) Offers information on the CoV of capacitance readings for increasing pressure. (iv) Shows the mean and standard deviation (error) of normalized capacitance under different amounts of pressure. The sensor's sensitivity is found to be non-linear, with some degree of linearity in different ranges. The linear ranges include low-pressure (1 – 5 *kPa*), moderate-pressure (25 *kPa* – 100 *kPa*), and high-pressure (150 *kPa* – 300 *kPa*). (C) Depicts the temporal response of the tactile sensor in four different types of surface with increasing pressure: (i) Response on plastic. (ii) Response on tile.(iii) Response on a sponge. (iv) Response on sand.

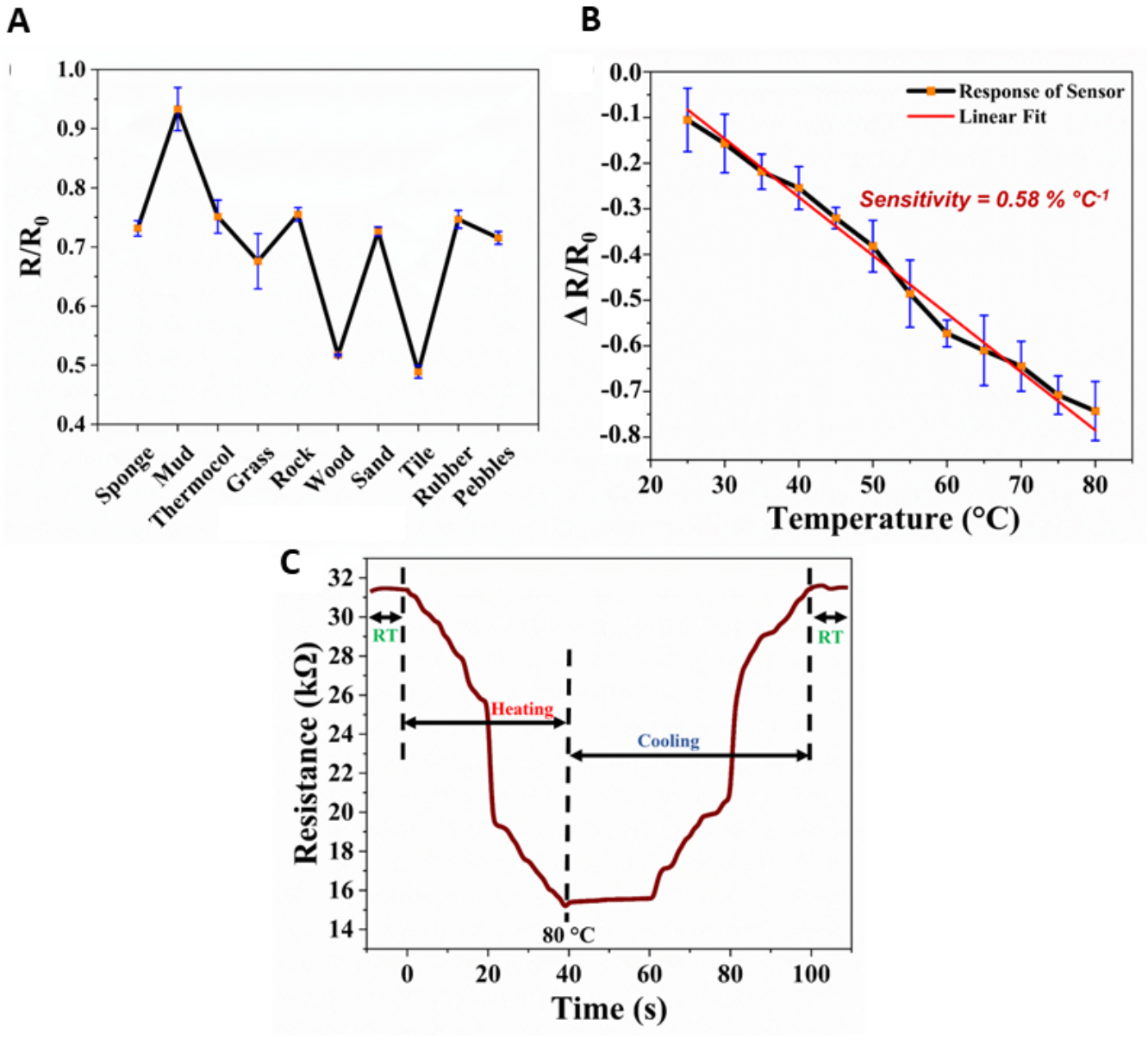

Figure 3. The results of experiments utilizing the GO + PEDOT:PSS temperature sensor are presented pllotted as follows: (A) Illustrates the response of the GO + PEDOT:PSS temperature sensor when placed 2 *mm* above different surfaces. Each surface exhibits a distinct radiative heat pattern. (B) The sensitivity of the sensor is calculated to be 0.58% $°C^{-1}$, demonstrating a linear characteristic. (C) The heating and cooling cycle is performed to assess any hysteresis in sensor response and to determine the sensor's response time.

perimental investigations involving various ZnO concentrations (0.5, 1, 2, 5, and 10 w/w% of PDMS) revealed that a 2 w/w% ratio yielded optimal electrical and mechanical responses. This concentration mitigates agglomeration issues and preserves the mechanical characteristics without hindering the curing process or compromising the composite's Young's modulus[36].

ZnO plays a crucial role in imparting linearity to the sensor response, and the incorporation of porous microstructures is intended to boost sensitivity through various mechanisms. Chiefly, these microstructures aid in distributing the applied load towards thinner regions of the material, thereby diminishing its modulus and encouraging compressibility[37]. Consequently, the material demonstrates increased compressive strain in response to a given pressure stimulus. Additionally, the buckling of these microstructures prompts air displacement across gaps, resulting in an augmented effective permittivity of the dielectric material[38]. This modification increases the volumetric ratio of the dielectric material with improved permittivity. Furthermore, the existence of viscoelasticity, a time-dependent stress-strain relationship inherent in certain elastic materials[39], introduces hysteresis, limiting the relaxation and response time of sensors. The incorporation of microstructuring techniques offers a means to mitigate the undesirable viscoelastic effects, thereby enhancing temporal resolution and further elevating sensor performance. These combined benefits underscore the crucial role of microstructural engineering in optimizing the sensitivity and temporal characteristics of tactile sensors. A comparison of various fabricated tactile sensors with ours is presented in Table 1D, clearly illustrating that the innovations introduced during the fabrication of this sensor position it well ahead of the other works.

Conductive organic polymers have attracted considerable interest as promising options for printed resistive temperature sensors due to their outstanding optical transparency and electrical conductivity[40]. The integration of graphene oxide (GO) has become a viable strategy to enhance the thermal activation capabilities of PEDOT:PSS as a temperature-sensitive layer[41]. Current sensors relying on PEDOT:PSS face challenges such as lower sensitivity (0.6 % $°C^{-1}$) and extended response and recovery times. To overcome these limitations, the intrinsic biocompatibility, insulating properties, and functional groups found in graphene oxide (GO) have been utilized to robustly functionalize the temperature-dependent PEDOT:PSS. This approach results in improved stability, enhanced sensitivity in temperature sensors, and unprecedented responsivity[28]. Various surfaces exhibit unique radiative patterns in their mean and standard deviation, as depicted in Figure 3A, although no discernible pattern is evident. Radiative heat flux is contingent on surface area and emissivity[42], and it displays variability across different surfaces. The sensitivity value obtained, while lower than what is reported in existing literature[28], stems from the difference in our approach, which involves characterizing the sensor using radiative heat rather than direct contact with the heating surface. This distinction contributes to the observed reduction in sensitivity. Nevertheless, the achieved sensitivity level remains notably higher than that reported for other polymer-based sensors documented in the literature.

The surface classification algorithm utilizes the Rectified Linear Unit (ReLU) activation function, a widely adopted choice in machine learning tasks due to its advantages, including enhanced optimization through stochastic gradient descent, efficient computation, and scale-invariance[43]. Backpropagation, a crucial technique for training Multilayer Perceptrons (MLPs), iteratively adjusts network weights to minimize the cost function. In each iteration, weighted sums propagate forward, and the gradient of the mean squared error (MSE) is computed for input-output pairs. This gradient is then used to update the weights of the first hidden layer, enabling backward propagation and facilitating the learning process. The mathematical expression for the weight update procedure is as follows[44]:

$$\Delta w(t) = -\varepsilon \frac{dE}{dw(t)} + \alpha \Delta w(t-1) \tag{1}$$

where $\Delta w(t)$ is the gradient in current iteration, ε is the bias, dE is the error, $dw(t)$ is the weight vector, α is the learning rate and $\Delta w(t-1)$ is the gradient in the previous iteration. Finally, the SoftMax activation function is employed to produce the final prediction. The algorithmic architecture has been fine-tuned to include an advanced Multilayer Perceptron (MLP) configuration characterized by a multi-tiered arrangement of interconnected neural layers. This architecture comprises five hidden layers, each with a distinct number of neurons: 4, 150, 200, 50, and 11, respectively. The initial layer, with its carefully chosen 4

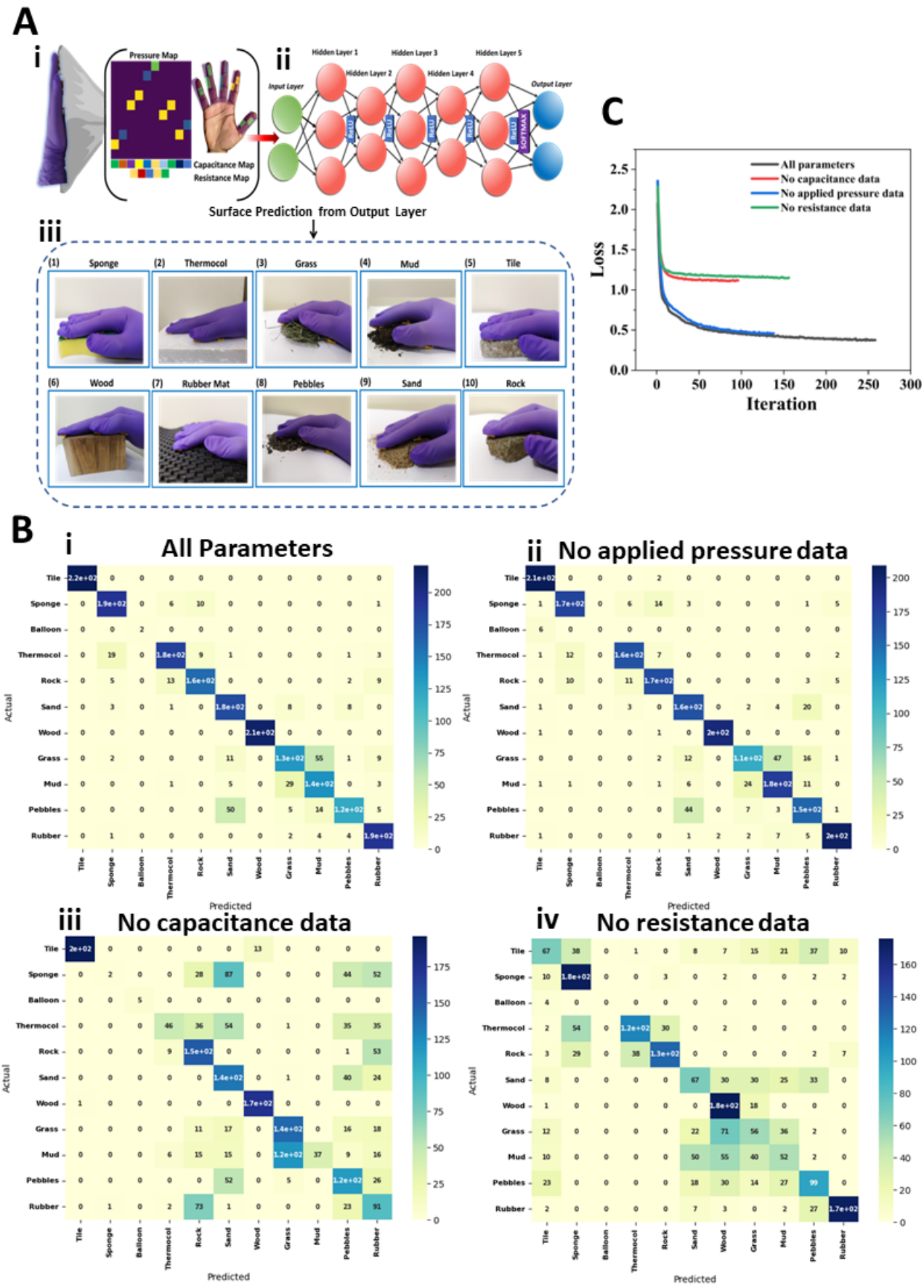
A
i
Pressure Map
Capacitance Map
Resistance Map
ii
Hidden Layer 1
Hidden Layer 2
Hidden Layer 3
Hidden Layer 4
Hidden Layer 5
Input Layer
Output Layer
RELU
SOFTMAX
Surface Prediction from Output Layer
iii
(1) Sponge
(2) Thermocol
(3) Grass
(4) Mud
(5) Tile
(6) Wood
(7) Rubber Mat
(8) Pebbles
(9) Sand
(10) Rock
C
All parameters
No capacitance data
No applied pressure data
No resistance data
Loss
Iteration
B
i All Parameters
ii No applied pressure data
iii No capacitance data
iv No resistance data
Actual
Predicted
Tile
Sponge
Balloon
Thermocol
Rock
Sand
Wood
Grass
Mud
Pebbles
Rubber

Figure 4. (A) A schematic summarizing the data collection and processing steps is outlined: (i) Real-time data collection occurs when the glove with sensors is placed on a surface. (ii) The collected data is transmitted to an MLP algorithm for prediction. (iii) The MLP algorithm generates a final output. (B) The confusion matrix for the 11 different surfaces is presented: (i) All parameters are considered. (ii) Applied pressure data is excluded, but the algorithm still performs reasonably well. (iii) Capacitance data is excluded. (iv) Resistance data is excluded. (C) Loss curves are plotted for four different cases to assess the learning rate.

neurons, effectively captures the comprehensive set of input features present in the dataset, while the final layer with 11 neurons precisely aligns with the distinctive number of classes inherent to our classification task.

Our work highlights the significant potential of a combined array of tactile and temperature sensors, transforming intelligent tactile sensing skin and advancing surface perception. The proposed sensing skin architecture is versatile, enabling simultaneous detection of various stimuli, including contact pressure and radiative heat emissions. Multiple touch sensors, designed to minimize cross-coupling effects, closely mimic sophisticated tactile perception like humanoid robot hands. Leveraging machine learning, particularly the MLP algorithm, gathered sensing data enables comprehensive characterization of surfaces, identifying topographical features accurately. Utilizing distinct radiative heat patterns and mechanical properties enhances surface perception accuracy and reliability, providing a nuanced understanding of the environment. Although our findings illustrate the effectiveness of the approach, our future work will focus on additional experimentation using a larger and more diverse sample set. Fine-tuning PDMS membrane thickness and exploring alternative materials can enhance sensor sensitivity and detection limits, considering cost and synthesis aspects. Personalized sensory feedback holds promise for future systems. In conclusion, our research offers insights into the potential of our sensor system for applications in human robot interactions and smart prosthetics, necessitating ongoing efforts to broaden investigations, refine algorithms, and foster robust, versatile intelligent perception systems.

Methods

Materials. The high-resolution grey resin (product code: RS-F2-GPGR-04) purchased from Formlabs was used to fabricate the micro-structured tactile sensor mold. Aluminum electrodes (Aluminium Solid PVC Wire Single Core) from Litost® and silver (Ag) paste (RS Pro Silver Conductive Paste, Liquid) from RS Components were used for establishing electrical contacts for both sensors. The temperature sensor used a well-balanced combination of GO solution (Graphene oxide paste, non-exfoliated) and the conducting polymer PEDOT:PSS (PEDOT:PSS 1.3 wt % dispersion in H_2O, conductive grade) as sensing material, while the tactile sensor used a mixture of PDMS-citric acid monohydrate (CAM) (reagent grade, $\geq$98%) and ZnO (ReagentPlus®, powder < 5 μm particle size, 99.9%) nanoparticles. The Ag paste, GO, PEDOT:PSS, and CAM were purchased from Sigma-Aldrich; the Kapton tape, used as a substrate for the temperature sensing material, was purchased from Essence Tape; and PDMS was purchased from Dow Corning.

Tactile sensor fabrication. The tactile sensor's porous sensing layer is comprised of ZnO nanoparticles having a diameter exceeding 100 nm. This is combined with PDMS and CAM particles, which introduce pores of approximately 100-200 μm in size. Utilized as the base material, PDMS imparts outstanding characteristics such as elasticity, stability, ease of fabrication, customizable features, and a dielectric constant (ε) of 2.7, as specified in the Sylgard-184® silicone material datasheet. The formulation involves a well-balanced mixture of PDMS:cross-linker weight ratio of 10:1 w/w%, a PDMS:CAM ratio of 3:1 w/w%, and 2% ZnO nanoparticles to total weight of mixture. After pouring the mixture into the mold, it underwent a curing process for 5 hours at 70°C. Subsequently, the material underwent immersion in deionized (DI) water for 24 hours to facilitate the breakdown of CAM, resulting in the desired porosity. After completing the de-molding and drying stages, Ag paste was meticulously applied to both faces of the ZnO-PDMS layer, constructed with dimensions of 10 mm × 10 mm × 2 mm (L×W×H), thereby finalizing the sensing layer. Following this, aluminum wires were connected to these surfaces, functioning as electrodes. A polyimide layer (Kapton tape) was applied as the sensor's substrate layer. The fabrication process and the resulting sensor are depicted in Figure 5A (i). The microstructures and pore size of the manufactured tactile sensor were examined through field emission scanning electron microscopy (FESEM), and the elemental composition of the sensor was methodically analyzed using Energy Dispersive X-Ray Spectroscopy (EDX), providing a thorough comprehension of its constituent elements. Visual representations are presented in Figure 5B (i), (ii), and (iii).

Temperature sensor fabrication. A commercially available PI substrate, approximately 60 μm in thickness, was precisely

sectioned into dimensions of 10 mm × 10 mm (L×W). To disperse the graphene oxide (GO) material, it underwent mild sonication in deionized (DI) water at a concentration of 1 mg/mL. To achieve optimal homogeneity, a blend of PEDOT:PSS and GO dispersion, in a 1:1 ratio, underwent thorough vortex mixing for 5 minutes. Subsequently, 20 μL of the GO+PEDOT:PSS ink was meticulously drop-cast onto the PI substrate to ensure uniform coverage. To mitigate the impact of external factors like humidity, an extra layer of PI was accurately added. The fabrication process details are illustrated in Figure 5A(ii), including microscopic images and elemental characterization for both sensors in Figure 5B(iii). FESEM and EDX were employed to visualize the microstructure and morphology of the GO+PEDOT:PSS thin film in the temperature sensor, along with the elemental composition of the film, as demonstrated in Figure 5B(iii).

Testbed setup and data. The comprehensive assessment of the fabricated tactile sensor included testing on various surfaces, coupled with the meticulous application of controlled pressure. The capacitance readings obtained were recorded using a HIOKI LCR meter (IM3536), as illustrated in Figure 5C. To ensure reliable comparisons, the recorded readings were subsequently normalized by dividing them by the reference capacitance (C/C_0). In the low-pressure range, calibrated weights ranging from 0.1 to 2 kPa were utilized. For investigating the sensor's response to higher pressures, a specially designed pressure application apparatus was developed, boasting exceptional resolution (0.2 kPa) and a maximum pressure capacity of 160 kPa. The data acquisition process comprised two distinct phases (static and dynamic), each tailored to extract specific insights. Precise capacitance readings were obtained using a microcontroller board (Arduino Mega 2560) as pressure increased gradually. The dynamic analysis, conducted on four distinct surfaces, facilitated an understanding of the temporal behavior and response characteristics of the tactile sensors, offering valuable insights into their performance dynamics. Alternatively, due to the dual sensitivity of GO + PEDOT:PSS to both pressure and temperature, utilizing resistance measurements alone with the DMM6500 Keithley Multimeter to ascertain surface temperature would lead to inaccuracies, given the intertwined effects of applied pressure. To address this constraint, a distinct temperature sensor was positioned near the tactile sensor, maintaining a non-contact distance of 2 mm (matching the thickness of the tactile sensor) from the surface, as depicted in Figure 5D. The resistance readings arising from radiative heat were then normalized and plotted to facilitate a thorough analysis. The sensor's normalized response was assessed consistently at a fixed height of 2 mm above various surfaces.

Machine learning. Significant optimization efforts were undertaken to enhance the performance of various classification-based machine learning methods. For classification purposes using the glove configuration within the Scikit-learn framework, a Multilayer Perceptron (MLP) network was devised. The MLP model comprises five fully connected hidden layers, each with a varying number of neurons, and non-linearity was introduced using rectified linear units (ReLU). The training dataset was employed for model training across 500 iterations, with the model's learning rate set at 0.001 for optimal performance. To determine the optimal number of neurons in the hidden layers, we initially kept the number of hidden layers constant at two and made adjustments to the number of neurons in each layer. Additionally, we refined the count of hidden layers in the model, recognizing its significant impact on classification accuracy.

Hardware for computing surface classification. The computational framework utilized for data acquisition, iterative training, and testing comprises an AMD Ryzen 7 6800H CPU boasting 8 cores and 16 logical processors. Additionally, the system is enhanced with an NVIDIA GeForce RTX 3060 GPU, featuring 6 GB of VRAM. Complementing this hardware, the system is equipped with 16 GB DDR5 4800 MHz physical memory (RAM). Furthermore, data accessibility and throughput were optimized through the utilization of a Micron 2450 NVMe 1TB SSD, improving the overall computational efficiency and data handling capabilities.

Calculation of the classification performance metrics. Accuracy and F_1 score are the two metrics used for surface classification performance evaluation. Accuracy is ascertained based on the true positives (TP), false positives (FP), true negatives (TN), and false negatives (FN) values, which are employed in the calculation of the accuracy measure defined in 2.

$$\text{Accuracy} = \left(\frac{TP+TN}{TP+FP+TN+FN} \right) \tag{2}$$

The F_1 score, being the harmonic mean of precision and recall, serves as a valuable performance measure. By considering both precision and recall, it provides a more nuanced assessment of our classification approach. The F_1 scores obtained are shown in Table 1C and the calculation is defined as in 3. The Precision and Recall are defined in 4 and 5 respectively.

$$F_1 \text{ score} = \left(\frac{2 \times \text{Precision} \times \text{Recall}}{\text{Precision} + \text{Recall}} \right) \tag{3}$$

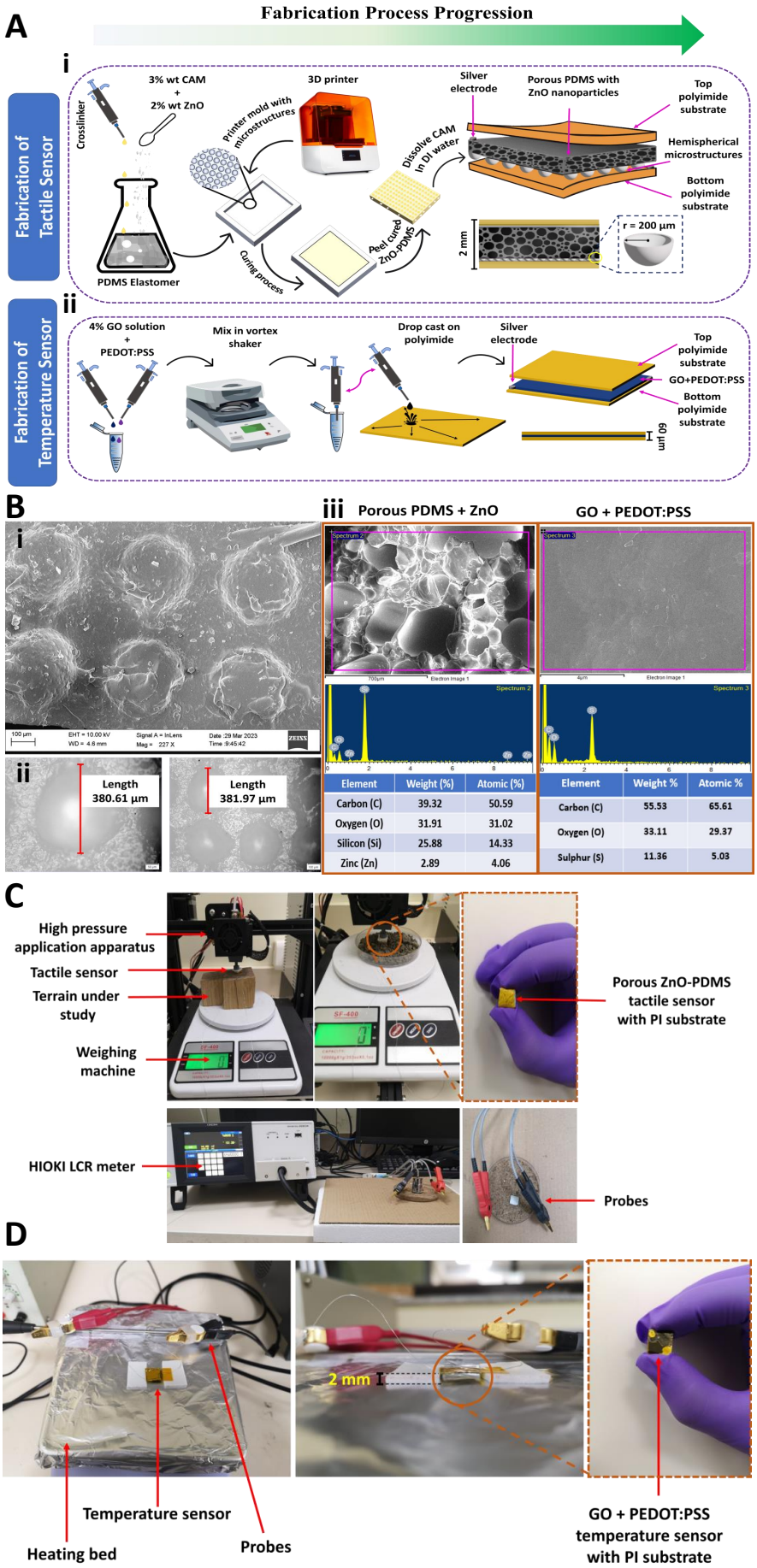
A
Fabrication Process Progression
i
Fabrication of Tactile Sensor
Crosslinker
3% wt CAM + 2% wt ZnO
3D printer
Printer mold with microstructures
PDMS Elastomer
Curing process
Peel cured ZnO-PDMS
Dissolve CAM in DI water
Silver electrode
Porous PDMS with ZnO nanoparticles
Top polyimide substrate
Hemispherical microstructures
Bottom polyimide substrate
2 mm
r = 200 µm
ii
Fabrication of Temperature Sensor
4% GO solution + PEDOT:PSS
Mix in vortex shaker
Drop cast on polyimide
Silver electrode
Top polyimide substrate
GO+PEDOT:PSS
Bottom polyimide substrate
60 µm
B
i
ii
Length 380.61 µm
Length 381.97 µm
iii
Porous PDMS + ZnO
GO + PEDOT:PSS
Element | Weight (%) | Atomic (%)
Carbon (C) | 39.32 | 50.59
Oxygen (O) | 31.91 | 31.02
Silicon (Si) | 25.88 | 14.33
Zinc (Zn) | 2.89 | 4.06
Element | Weight % | Atomic %
Carbon (C) | 55.53 | 65.61
Oxygen (O) | 33.11 | 29.37
Sulphur (S) | 11.36 | 5.03
C
High pressure application apparatus
Tactile sensor
Terrain under study
Weighing machine
Porous ZnO-PDMS tactile sensor with PI substrate
HIOKI LCR meter
Probes
D
2 mm
Temperature sensor
Heating bed
Probes
GO + PEDOT:PSS temperature sensor with PI substrate

Figure 5. (A) The fabrication process of the flexible tactile and temperature sensors is described: (i) Illustration of the ZnO-PDMS porous tactile sensor. (ii) Illustration of the GO + PEDOT:PSS flexible temperature sensor, along with the final sensor schematic. (B) FESEM and EDX analysis of the tactile and temperature sensor: (i) and (ii) Depiction of the hemispherical microstructures on the face of the tactile sensor with a diameter of $\sim$400 μm. (iii) Presentation of the dimensions of pores ($\sim$200 μm) and elemental characterization of the tactile sensor through FESEM and EDX. Formation of GO + PEDOT:PSS thin film on a PI substrate and its corresponding elemental characterization for the temperature sensor through FESEM and EDX. (C) The experimental setup and fabricated sensor are shown. It includes custom-made pressure application apparatus used to apply high pressure on surface, wood, and soil; close-up view of the fabricated sensor; illustration of how the LCR meter was used to obtain capacitance readings when calibrated weights were used to apply low pressure; and close-up view of the sensor on a surface. (D) Experimental setup for observing the response of the temperature sensor under radiative heat. It includes: components involved in the setup; placement of the sensor at a height of 2 *mm* above the surface; and the fabricated sensor held in hand.

$$\text{Precision} = \left(\frac{TP}{TP+FP} \right) \tag{4}$$

$$\text{Recall} = \left(\frac{TP}{TP+FN} \right) \tag{5}$$

Data Availability

The data substantiating the plots presented in this article, along with other findings from this research, can be obtained upon request from the corresponding author.

Code Availability

The code will be made available upon a reasonable request directed to the corresponding author.

References

1. Silvera-Tawil, D., Rye, D. & Velonaki, M. Artificial skin and tactile sensing for socially interactive robots: A review. *Robotics Auton. Syst.* **63**, 230–243, DOI: 10.1016/j.robot.2014.09.008 (2015).
2. Wu, Y. *et al.* A skin-inspired tactile sensor for smart prosthetics. *Sci. Robotics* **3**, DOI: 10.1126/scirobotics.aat0429 (2018).
3. Nampoothiri, M. G. H., Vinayakumar, B., Sunny, Y. & Antony, R. Recent developments in terrain identification, classification, parameter estimation for the navigation of autonomous robots. *SN Appl. Sci.* **3**, DOI: 10.1007/s42452-021-04453-3 (2021).
4. Al-dabbagh, A. H. & Ronsse, R. A review of terrain detection systems for applications in locomotion assistance. *Robotics Auton. Syst.* **133**, 103628, DOI: 10.1016/j.robot.2020.103628 (2020).
5. Seo, D.-G. *et al.* Versatile neuromorphic electronics by modulating synaptic decay of single organic synaptic transistor: From artificial neural networks to neuro-prosthetics. *Nano Energy* **65**, 104035, DOI: 10.1016/j.nanoen.2019.104035 (2019).
6. Atzori, M., Cognolato, M. & Müller, H. Deep learning with convolutional neural networks applied to electromyography data: A resource for the classification of movements for prosthetic hands. *Front. Neurorobotics* **10**, DOI: 10.3389/fnbot.2016.00009 (2016).
7. Rovira-Más, F., Zhang, Q. & Reid, J. F. Stereo vision three-dimensional terrain maps for precision agriculture. *Comput. Electron. Agric.* **60**, 133–143, DOI: 10.1016/j.compag.2007.07.007 (2008).
8. Ponticelli, R. & de Santos, P. G. Obtaining terrain maps and obstacle contours for terrain-recognition tasks. *Mechatronics* **20**, 236–250, DOI: 10.1016/j.mechatronics.2009.11.008 (2010).
9. Surmann, H., Nüchter, A. & Hertzberg, J. An autonomous mobile robot with a 3d laser range finder for 3d exploration and digitalization of indoor environments. *Robotics Auton. Syst.* **45**, 181–198, DOI: 10.1016/j.robot.2003.09.004 (2003).

10. Demolder, C., Molina, A., Hammond, F. L. & Yeo, W.-H. Recent advances in wearable biosensing gloves and sensory feedback biosystems for enhancing rehabilitation, prostheses, healthcare, and virtual reality. *Biosens. Bioelectron.* **190**, 113443, DOI: 10.1016/j.bios.2021.113443 (2021).

11. Rautaray, S. S. & Agrawal, A. Vision based hand gesture recognition for human computer interaction: a survey. *Artif. Intell. Rev.* **43**, 1–54, DOI: 10.1007/s10462-012-9356-9 (2012).

12. Kim, M., Cho, J., Lee, S. & Jung, Y. Imu sensor-based hand gesture recognition for human-machine interfaces. *Sensors* **19**, 3827, DOI: 10.3390/s19183827 (2019).

13. Lee, J. *et al.* Conductive fiber-based ultrasensitive textile pressure sensor for wearable electronics. *Adv. Mater.* **27**, 2433–2439, DOI: 10.1002/adma.201500009 (2015).

14. Bai, H. *et al.* Stretchable distributed fiber-optic sensors. *Science* **370**, 848–852, DOI: 10.1126/science.aba5504 (2020).

15. Liang, C., Sun, F. & Rogers, C. Coupled electro-mechanical analysis of adaptive material systems — determination of the actuator power consumption and system energy transfer. *J. Intell. Material Syst. Struct.* **5**, 12–20, DOI: 10.1177/1045389x9400500102 (1994).

16. Zhao, J., Lee, V. E., Liu, R. & Priestley, R. D. Responsive polymers as smart nanomaterials enable diverse applications. *Annu. Rev. Chem. Biomol. Eng.* **10**, 361–382, DOI: 10.1146/annurev-chembioeng-060718-030155 (2019).

17. Tajik, S. *et al.* Recent developments in conducting polymers: applications for electrochemistry. *RSC Adv.* **10**, 37834–37856, DOI: 10.1039/d0ra06160c (2020).

18. Wan, M. *Conducting polymers with micro or nanometer structure* (Springer Berlin Heidelberg, 2008).

19. Nezakati, T., Seifalian, A., Tan, A. & Seifalian, A. M. Conductive polymers: Opportunities and challenges in biomedical applications. *Chem. Rev.* **118**, 6766–6843, DOI: 10.1021/acs.chemrev.6b00275 (2018).

20. Ravichandran, R., Sundarrajan, S., Venugopal, J. R., Mukherjee, S. & Ramakrishna, S. Applications of conducting polymers and their issues in biomedical engineering. *J. The Royal Soc. Interface* **7**, DOI: 10.1098/rsif.2010.0120.focus (2010).

21. Le, T.-H., Kim, Y. & Yoon, H. Electrical and electrochemical properties of conducting polymers. *Polymers* **9**, 150, DOI: 10.3390/polym9040150 (2017).

22. Chen, S. & Guo, X. Improving the sensitivity of elastic capacitive pressure sensors using silver nanowire mesh electrodes. *IEEE Transactions on Nanotechnol.* **14**, 619–623, DOI: 10.1109/tnano.2015.2422993 (2015).

23. Tang, Q., Zou, M., Chang, L. & Guo, W. A super-flexible and transparent wood film/silver nanowire electrode for optical and capacitive dual-mode sensing wood-based electronic skin. *Chem. Eng. J.* **430**, 132152, DOI: 10.1016/j.cej.2021.132152 (2022).

24. Cicek, M. O., Doganay, D., Durukan, M. B., Gorur, M. C. & Unalan, H. E. Seamless monolithic design for foam based, flexible, parallel plate capacitive sensors. *Adv. Mater. Technol.* **6**, DOI: 10.1002/admt.202001168 (2021).

25. Cheng, Y., Wang, R., Zhai, H. & Sun, J. Stretchable electronic skin based on silver nanowire composite fiber electrodes for sensing pressure, proximity, and multidirectional strain. *Nanoscale* **9**, 3834–3842, DOI: 10.1039/c7nr00121e (2017).

26. Zhao, X.-F. *et al.* Hollow mxene sphere-based flexible e-skin for multiplex tactile detection. *ACS Appl. Mater. amp; Interfaces* **13**, 45924–45934, DOI: 10.1021/acsami.1c06993 (2021).

27. Singh, L., Tripathy, K. & Bhattacharjee, M. Porous microstructure-assisted flexible and highly sensitive polymer piezoresistive pressure sensor. *Adv. Eng. Mater.* **24**, DOI: 10.1002/adem.202200500 (2022).

28. Soni, M., Bhattacharjee, M., Ntagios, M. & Dahiya, R. Printed temperature sensor based on pedot: Pss-graphene oxide composite. *IEEE Sensors J.* **20**, 7525–7531, DOI: 10.1109/jsen.2020.2969667 (2020).

29. Ramadan, K. S., Sameoto, D. & Evoy, S. A review of piezoelectric polymers as functional materials for electromechanical transducers. *Smart Mater. Struct.* **23**, 033001, DOI: 10.1088/0964-1726/23/3/033001 (2014).

30. Wang, Z. Novel nanostructures of zno for nanoscale photonics, optoelectronics, piezoelectricity, and sensing. *Appl. Phys. A* **88**, 7–15, DOI: 10.1007/s00339-007-3942-8 (2007).

31. Singh, A. *et al.* Low cost fabrication of polymer composite (h-zno + pdms) material for piezoelectric device application. *Mater. Res. Express* **3**, 075702, DOI: 10.1088/2053-1591/3/7/075702 (2016).

32. Charde, S. J. *et al.* Copper-doped zinc oxide nanoparticles: Influence on thermal, thermo mechanical, and tribological properties of polycarbonate. *Polym. Compos.* **39**, DOI: 10.1002/pc.24315 (2017).

33. Saadattalab, V., Shakeri, A. & Gholami, H. Effect of cnts and nano zno on physical and mechanical properties of polyaniline composites applicable in energy devices. *Prog. Nat. Sci. Mater. Int.* **26**, 517–522, DOI: 10.1016/j.pnsc.2016.09.005 (2016).

34. Cho, K. S., Hong, J. & Chung, C. I. Effects of zno nano particles on thermal stabilization of polymers. *Polym. Eng. amp; Sci.* **44**, 1702–1706, DOI: 10.1002/pen.20170 (2004).

35. Zhao, S. & Zhu, R. High sensitivity and broad range flexible pressure sensor using multilayered porous pdms/agnp sponge. *Adv. Mater. Technol.* **4**, DOI: 10.1002/admt.201900414 (2019).

36. Kutvonen, A., Rossi, G., Puisto, S. R., Rostedt, N. K. J. & Ala-Nissila, T. Influence of nanoparticle size, loading, and shape on the mechanical properties of polymer nanocomposites. *The J. Chem. Phys.* **137**, DOI: 10.1063/1.4767517 (2012).

37. Tee, B. C. *et al.* Tunable flexible pressure sensors using microstructured elastomer geometries for intuitive electronics. *Adv. Funct. Mater.* **24**, 5427–5434, DOI: 10.1002/adfm.201400712 (2014).

38. Ruth, S. R. A. & Bao, Z. Designing tunable capacitive pressure sensors based on material properties and microstructure geometry. *ACS Appl. Mater. amp; Interfaces* **12**, 58301–58316, DOI: 10.1021/acsami.0c19196 (2020).

39. Deguchi, S., Hotta, J., Yokoyama, S. & Matsui, T. S. Viscoelastic and optical properties of four different pdms polymers. *J. Micromechanics Microengineering* **25**, 097002, DOI: 10.1088/0960-1317/25/9/097002 (2015).

40. Ghosal, A. & Kaushik, A. *Intelligent hydrogels in diagnostics and therapeutics* (CRC Press, 2020).

41. Pullanchiyodan, A., Manjakkal, L., Dervin, S., Shakthivel, D. & Dahiya, R. Metal coated conductive fabrics with graphite electrodes and biocompatible gel electrolyte for wearable supercapacitors. *Adv. Mater. Technol.* **5**, DOI: 10.1002/admt.201901107 (2020).

42. Bryant, R., Womeldorf, C., Johnsson, E. & Ohlemiller, T. Radiative heat flux measurement uncertainty. *Fire Mater.* **27**, 209–222, DOI: 10.1002/fam.822 (2003).

43. Si, J., Harris, S. L. & Yfantis, E. A dynamic relu on neural network. In *2018 IEEE 13th Dallas Circuits and Systems Conference (DCAS)*, 1–6, DOI: 10.1109/dcas.2018.8620116 (IEEE, 2018).

44. Singarimbun, R. N., Nababan, E. B. & Sitompul, O. S. Adaptive moment estimation to minimize square error in backpropagation algorithm. In *2019 International Conference of Computer Science and Information Technology (ICoSNIKOM)*, 1–7, DOI: 10.1109/icosnikom48755.2019.9111563 (IEEE, 2019).

Acknowledgements

This work has been supported in part by SERB SUPRA grant no. SPR/2020/000184, Government of India. The authors would also like to thank the Department of Electrical Engineering and Computer Science, Indian Institute of Science Education and Research, Bhopal.

Author contributions statement

The study was conceptualized by S.D., M.B., and K.T. Method development was undertaken by S.D and M.B. S.D. was responsible for coding, data analysis, curation, and validation. Experimental design and data interpretation was provided by M.B., K.T., and S.K. All authors actively contributed to the manuscript drafting, reviewing, and approval of the final manuscript for submission.

Competing interests

The authors declare no competing interests.

Additional information

Correspondence and requests for materials should be addressed to Mitradip Bhattacharjee.